Available online at www.sciencedirect.com

ScienceDirect

Journal of Nuclear Materials 375 (2008) 26–37

journal of nuclear materials

www.elsevier.com/locate/jnucmat

Radiation response of a 9 chromium oxide dispersion strengthened steel to heavy ion irradiation

T.R. Allen [a,*], J. Gan [b], J.I. Cole [b], M.K. Miller [c], J.T. Busby [c],
S. Shutthanandan [d], S. Thevuthasan [d]

[a] *University of Wisconsin, 1500 Engineering Drive, Madison, WI 53706, USA*
[b] *Idaho National Laboratory, USA*
[c] *Oak Ridge National Laboratory, USA*
[d] *Pacific Northwest National Laboratory, USA*

Received 15 September 2007; accepted 5 November 2007

Abstract

Ferritic–martensitic (FM) alloys are expected to play an important role as cladding or structural components in Generation IV systems operating in the temperature range 350–700 °C and to doses up to 200 dpa. Oxide dispersion strengthened (ODS) ferritic–martensitic steels have been developed to operate at higher temperatures than traditional FM steels. These steels contain nanometer-sized Y–Ti–O nanoclusters as a strengthening mechanism. Heavy ion irradiation has been used to determine the nanocluster stability over a temperature range of 500–700 °C to doses of 150 dpa. At all temperatures, the average nanocluster size decreases but the nanocluster density increases. The increased density of smaller nanoclusters under radiation should lead to strengthening of the matrix. While a reduction in size under irradiation has been reported in some other studies, many report oxide stability. The data from this study are contrasted to the available literature to highlight the differences in the reported radiation response.

1. Introduction

Advanced nuclear energy systems proposed under the Generation IV initiative are aimed at making revolutionary improvements in economics, safety and reliability, and sustainability. To achieve these advancements, Generation IV systems anticipate operating at much higher temperatures and to higher radiation damage than current light water reactors. Of the candidate alloy systems being considered, ferritic–martensitic alloys are expected to play an important role as cladding or structural components in Generation IV systems operating in the temperature range 350–700 °C and to doses up to 200 dpa [1–3].

Ferritic–martensitic steels offer better swelling resistance than austenitic steels but may suffer from grain boundary and/or matrix creep and loss of strength at temperatures above ~600 °C. However, specific, tailored microstructure modifications may be able to address the deficiencies at high temperature and dose. The martensitic 9Cr-ODS steel, oxide dispersion strengthened by mechanically alloying with Y_2O_3 particles, is designed for high creep strength at higher temperature. However, the stability of the oxide particles under irradiation to very high dose needs to be understood. Heavy ion irradiation provides a unique approach in this exploratory task to evaluate material tolerance to radiation up to very high doses.

2. Experiment

A bar of 9Cr-ODS ferritic steel (24 mm diameter and 60 mm length) was supplied by the Japan Nuclear Cycle Development Institute (now the Japan Atomic Energy Agency). The alloy had been annealed at 1050 °C for 60 min and subsequently tempered at 800 °C for 60 min.

---

[*] Corresponding author. Tel.: +1 608 265 4083.
E-mail address: allen@engr.wisc.edu (T.R. Allen).

0022-3115/$ - see front matter © 2007 Elsevier B.V. All rights reserved.
doi:10.1016/j.jnucmat.2007.11.001

The composition of 9Cr-ODS is listed in Table 1. The detailed manufacture process was described by Ohtuska et al. [4].

Prior to irradiation the alloy was characterized with the Oak Ridge National Laboratory's local electrode atom probe [5]. A specimen temperature of 60 K, a pulse repetition rate of 200 kHz and a pulse fraction of 20% were used for the analyses. Nanoclusters were located in the three-dimensional data by searching for those atoms within a certain distance of another solute atom of the same type [6]. This maximum separation or friends-of-friends (FOF) [7] method enables the solutes in the nanoclusters to be distinguished from the solutes in the matrix so that their size, composition and number density can be estimated. The magnitude of the separation distance depends on the solute concentrations in the nanoclusters and the matrix. A maximum separation distance of 0.6 nm was used in this study. This method detects solute agglomerations containing 2 or more atoms of interest. As some of the smaller agglomerations are due to the solute distribution in a random solid solution, a minimum size cutoff limit of 20 atoms was used to eliminate these regions. The center of mass, the radius of gyration, l_g, and the Guinier radius, r_G, may be estimated directly from the coordinates of the solute atoms in each nanocluster [8]. The number density, N_v, may be estimated from the number of nanoclusters in the analyzed volume and its volume as estimated from the total number of atoms in the volume and their atomic volumes [8].

The compositions of these nanoclusters were estimated with the envelope method [8]. In this method, a three-dimensional grid of volume elements containing the number of atoms of all elements with a grid spacing of 0.1 nm was constructed from the volume elements corresponding to the positions of the selected atom species. The solute concentrations may be determined by counting the number of atoms of each element within this three-dimensional envelope. It should be noted that at the size range of the nanoclusters found in these materials, i.e., less than 5 nm in diameter, the composition estimates of these nanoclusters are strongly dependent on many factors. The composition estimate depends on the definition of the position of the interface between the nanocluster and the matrix, the solute gradient into the matrix, the roughness of this interface on an atomic scale, and the presence and extent of interfacial segregation of all solutes.

For irradiation, thin sheet samples with a size roughly at $1.5 \times 1.5\ \text{cm}^2$ and a thickness approximately 200 μm were prepared, with a final surface polished using 0.1 μm diamond paste. The Ni ion irradiations were conducted at the Environmental and Molecular Science Laboratory at Pacific Northwest National Laboratory using 5 MeV Ni ions at 500, 600, and 700 °C and 1×10^{-7} torr with a damage rate of 1.4×10^{-3} dpa/s. The samples were mounted on a radiation stage that allows temperature control through heating with electron beam and cooling with liquid nitrogen flow in the cooling channel. The ion beam was rastered over an irradiated area of $8 \times 8\ \text{mm}^2$ on the sample. A rastered beam, rather than defocused beam, was used because the rastered beam covered a large area (sample + apertures equivalent to approximately 15 mm × 15 mm) with uniform beam intensity. The ion beam size diameter is approximately 1.5 mm. The accelerator used does not permit a beam size larger than 7 mm diameter through defocusing. An additional disadvantage of using a defocused beam is the non-uniform beam intensity due to the Gaussian distribution of the beam intensity in radial direction. Due to the relatively low ion beam current, the effect of beam on the sample temperature is anticipated to be very small.

The Ni ion irradiation used a beam current of 270 nA on the sample, a beam scanning horizontal frequency of 64 Hz and vertical frequency of 517 Hz. The quoted dpa rate is based on the average Ni ion particle flux and the SRIM displacement calculation with full detailed, full cascade calculation and a 40 eV displacement energy for Fe and Cr. Irradiation temperature was monitored using both a pyrometer and a thermocouple. The material was irradiated to doses up to 150 dpa.

Fig. 1 plots the damage profile and implanted ion profile as generated using SRIM [9] for 5 MeV Ni ions. The highlighted zone at 0.5 μm below the surface is the location from which the TEM samples were prepared. An ~100 nm thick slab is taken at 0.5 μm depth for TEM analysis to obtain reasonable radiation damage and also minimize the influence from the injected Ni interstitials.

Transmission electron microscopy (TEM) discs were punched using a disc punch to a diameter of 2.3 mm. The discs were then mechanically wet polished from the unirradiated side down to roughly 70 μm to minimize the magnetic interference with the electron beam in the microscope. A thin layer of approximately 0.5 μm depth was removed from the irradiated side using a 5-s jet electro-polishing with a solution of 2% perchloric acid and 15% ethylene glycol in methanol at a polishing condition of 25 V and −65 °C. TEM discs were then jet-polished from the unirradiated side to perforation. The 2.3 mm disc sample was mounted to a 50 μm thick and 3-mm diameter Cu slot grid using epoxy to provide a 3 mm diameter TEM disc. Microstructure characterization was carried out using a 200 kV transmission electron microscope equipped with EDS for chemical analysis.

Table 1
Nominal chemical composition of 9Cr-ODS alloys investigated in this study (wt%, bal. Fe)

Alloy	C	Mn	P	S	Si	Ni	Cr	N	Al	W	Ti	Y
ODS[a]	.14	.05	<.005	.003	.048	.06	8.6	.017	–	2	.21	.28

[a] $[\text{Y}_2\text{O}_3] = 1.27 \times [\text{Y}] = 0.36$; $[\text{Ex.O}] = [\text{Total O}]–[\text{O in Y}_2\text{O}_3\ \text{powder}] = [\text{O}] - 0.27 \times [\text{Y}]$.

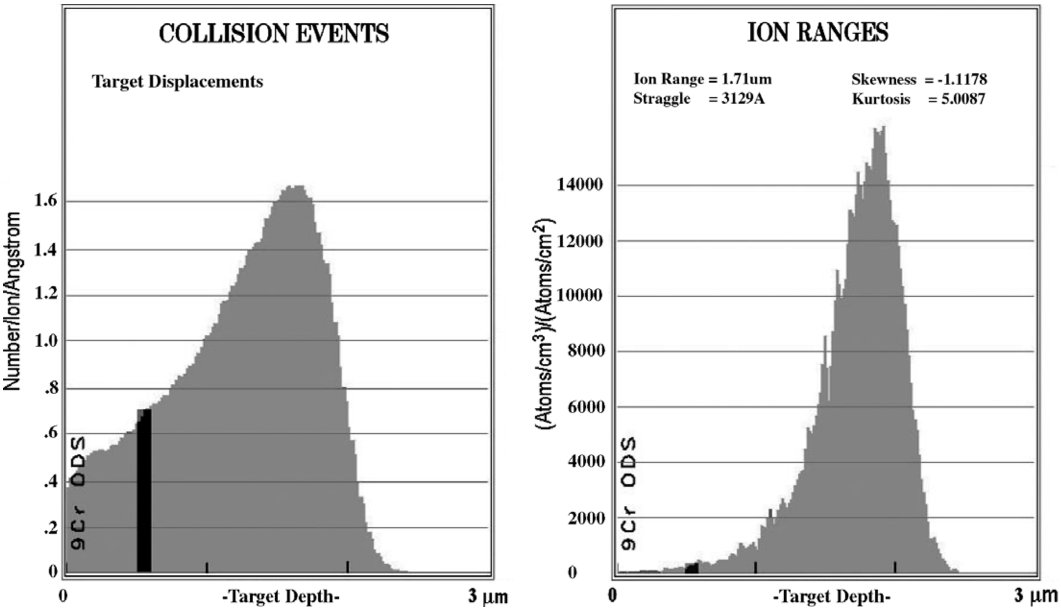

Fig. 1. SRIM plots comparing the damage profile with the implanted Ni-atom profile. TEM sample location was chosen to minimize any effect of implanted ions.

3. Results

Atom maps revealed the presence of titanium-, yttrium- and oxygen-enriched nanoclusters in the matrix, as shown in Fig. 2. These nanoclusters were similar to those previously observed by atom probe tomography in mechanically alloyed, oxygen dispersion strengthened (MA/ODS) 12YWT, 14YWT and MA957 alloys [3,8,10–16]. The average Guinier diameter, $2r_G$, of these nanoclusters was estimated from the maximum separation method to be $2r_G = 4.6$ nm. Their number density was estimated to be approximately $1.5 \times 10^{23}\ \mathrm{m}^{-3}$. The average composition of these nanoclusters was Fe–5% Cr, 5% Y, 32% Ti, and 35% O (all at.%). The grain boundaries were enriched in chromium, carbon and tungsten, as shown in the concentration profiles in Fig. 3. Similar behavior has also been

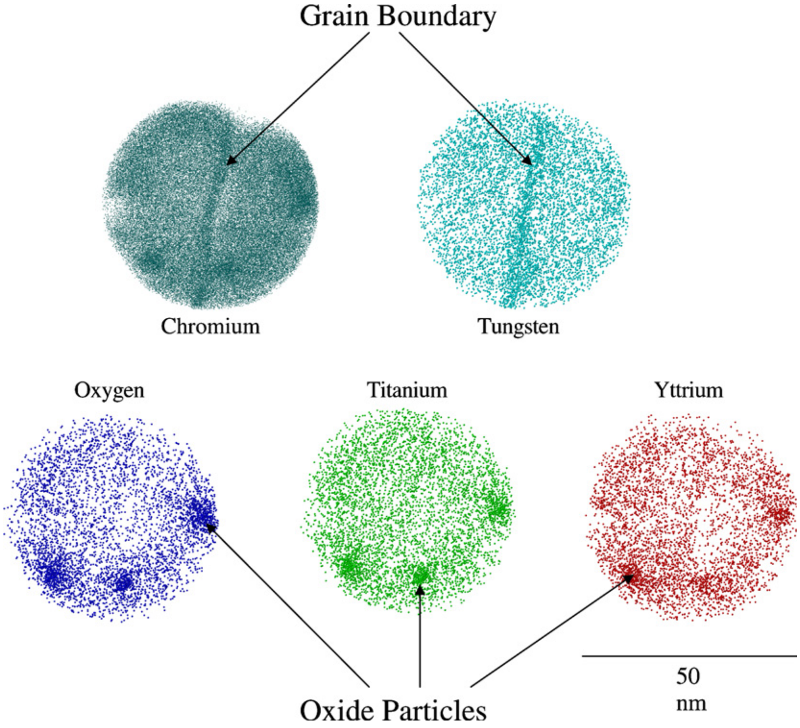

Fig. 2. Electron microprobe results indicate Cr and W enrichment at the grain boundary as well as Ti–O–Y rich clusters in the matrix.

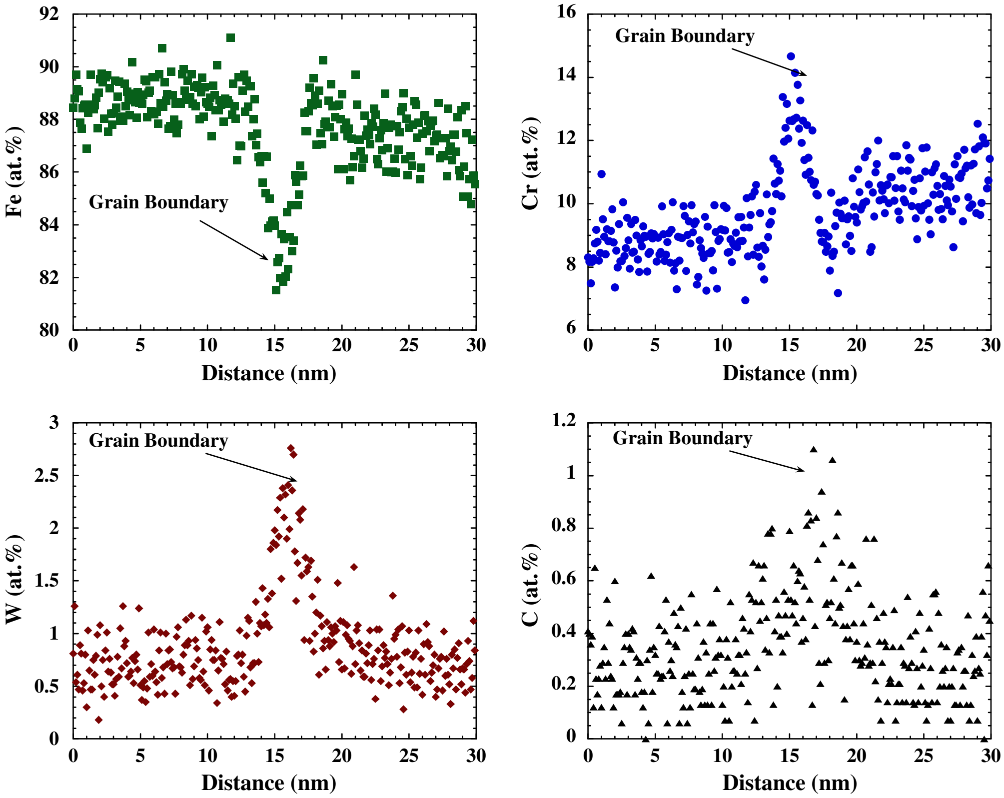

Fig. 3. Atom probe results indicate Cr, C and W enrichment, as well as Fe depletion, at the grain boundary.

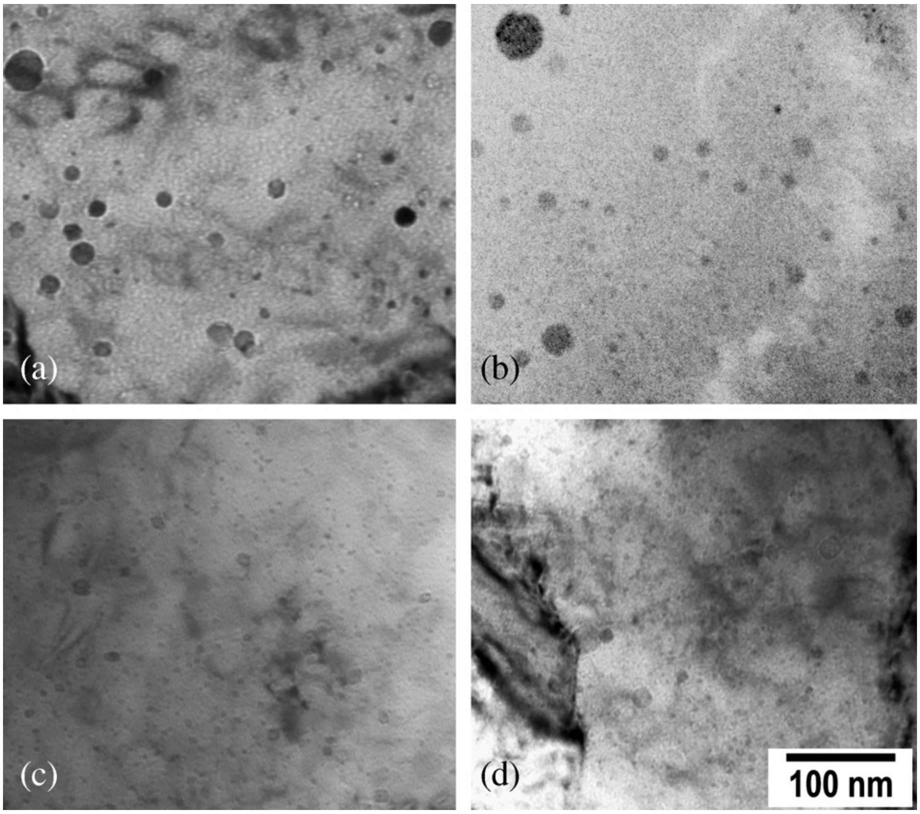

Fig. 4. Bright field image of yttrium–titanium-oxide particles, irradiated at 500 °C to: (a) 0 dpa, (b) 5 dpa, (c) 50 dpa and (d) 150 dpa, increase in density and decrease in size as dose increases [20].

observed in the other MA/ODS alloys. Cr enrichment on unirradiated grain boundaries is also typical in other ferritic–martensitic steels [17,18].

Typical bright field micrographs of the ODS material as a function of radiation dose are shown in Fig. 4 where the representative nanocluster particles are shown for samples irradiated at 500 °C to doses of 0, 5, 50, and 150 dpa. As the total radiation dose increases, the average nanocluster size decreases and the density of nanocluster particles increases. Bright field images taken away from any strongly excited diffraction were used to reveal nanocluster particles without interference from the dislocation images. For both the unirradiated and the irradiated conditions, EDS analysis indicates that the nanocluster particles were associated with high Ti at an atomic ratio close to 1:1 with Y. According to the work by Yamashita, et al. [19], these particles are mostly $Y_2Ti_2O_7(Y_2O_3–2TiO_2)$ oxide complex.

The average size, particle density, total particle volume, and number of particles characterized are listed in Table 2 for each irradiation condition. The average nanocluster size as a function of radiation dose for all three experimental temperatures is plotted in Fig. 5. At all temperatures, the average nanocluster particle decreases with increasing dose. At higher temperature (600–700 °C), the average size appears to reach an asymptotic value of approximately 5 nm. The density (number of particles per unit volume) of the nanocluster particles as a function of dose is displayed in Fig. 6. For all three temperatures the density increases with radiation dose. The largest increase is seen at the intermediate temperature of 600 °C. The mean nanocluster volume (the average volume of an individual nanocluster particle) decreases with radiation as the average particle size decreases. Fig. 7 plots the nanocluster volume fraction as a function of dose at all three temperatures. Due to limitations on available beam time, irradiations were not carried out to higher doses at 600 °C. At 600 and 700 °C, at increasing

Table 2
Oxide particle distribution descriptive statistics

Dose	Mean diameter (nm)	Mean volume (nm^3)	Measurements	Oxide density (m^{-3})
T = 500 °C				
0	11.7	1392	505	3.4E+21
5	10.5	1301	469	4.1E+21
50	10.1	984	295	4.7E+21
150	9.3	820	423	5.5E+21
T = 600 °C				
0	11.7	1392	505	3.4E+21
5	7.3	417	1146	1.2E+22
50	4.8	122	1009	1.9E+22
T = 700 °C				
0	11.7	1392	505	3.4E + 21
5	6.9	358	445	6.7E + 21
50	4.9	118	887	7.5E + 21
150	4.9	147	601	1.6E + 22

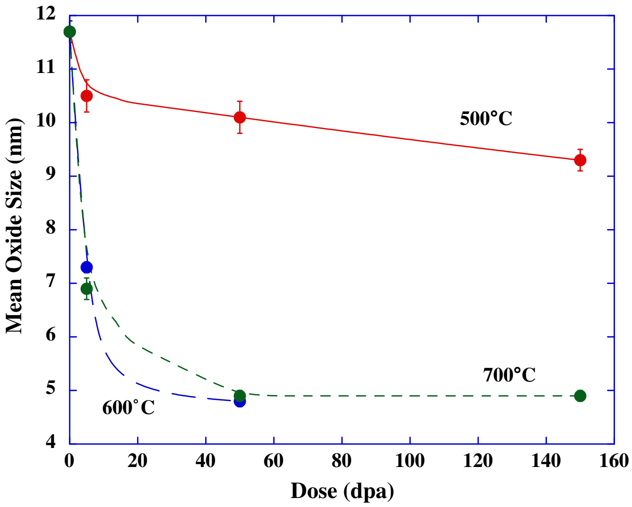

Fig. 5. Mean oxide diameter as a function of dose for samples irradiated at 500, 600, and 700 °C.

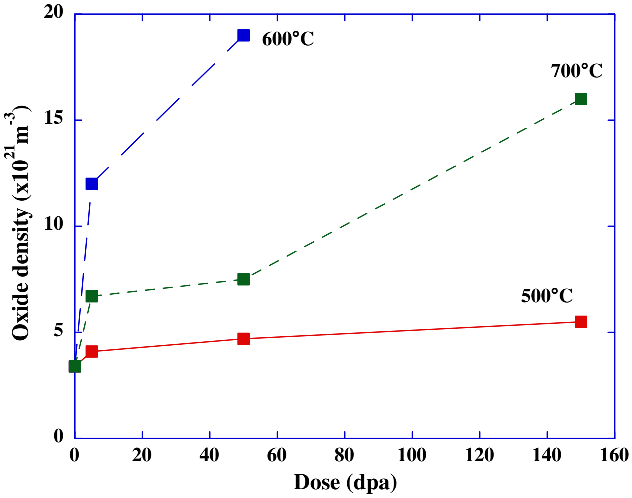

Fig. 6. Oxide density as a function of dose for samples irradiated at 500, 600, and 700 °C.

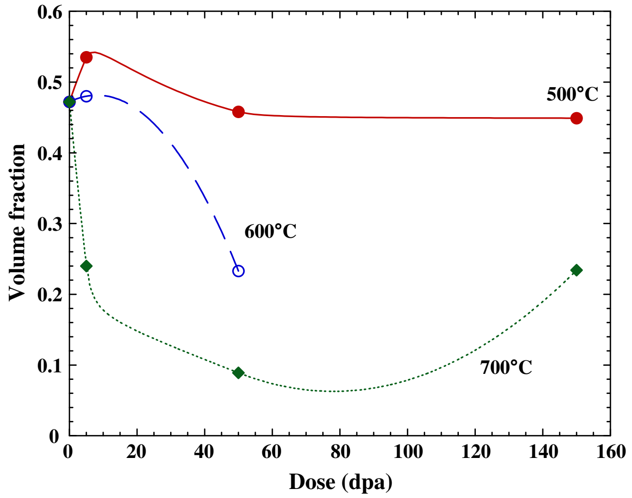

Fig. 7. Oxide volume fraction as a function of dose for samples irradiated at 500, 600, and 700 °C.

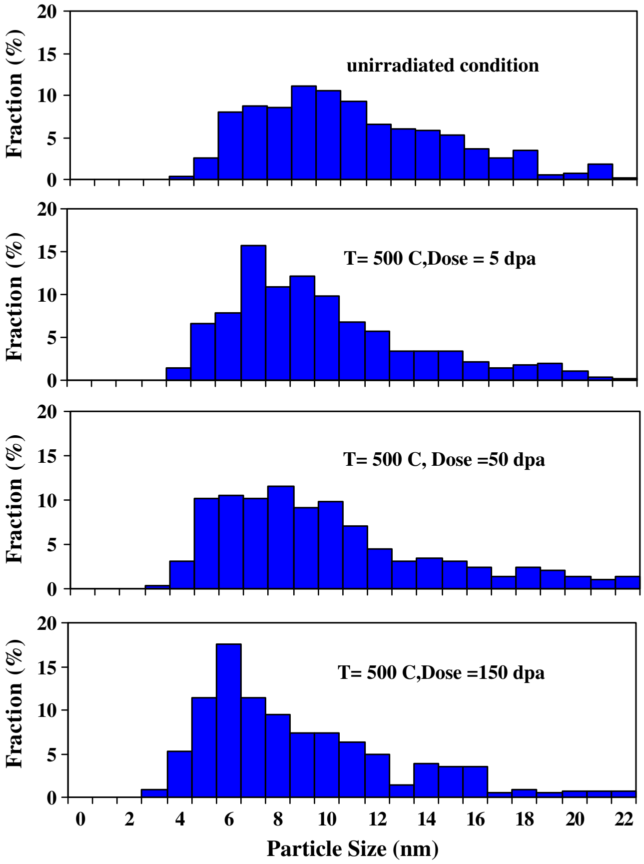

Fig. 8. Particle size (diameter) distribution for samples irradiated at 500 °C to doses of 0, 5, 50, and 150 dpa.

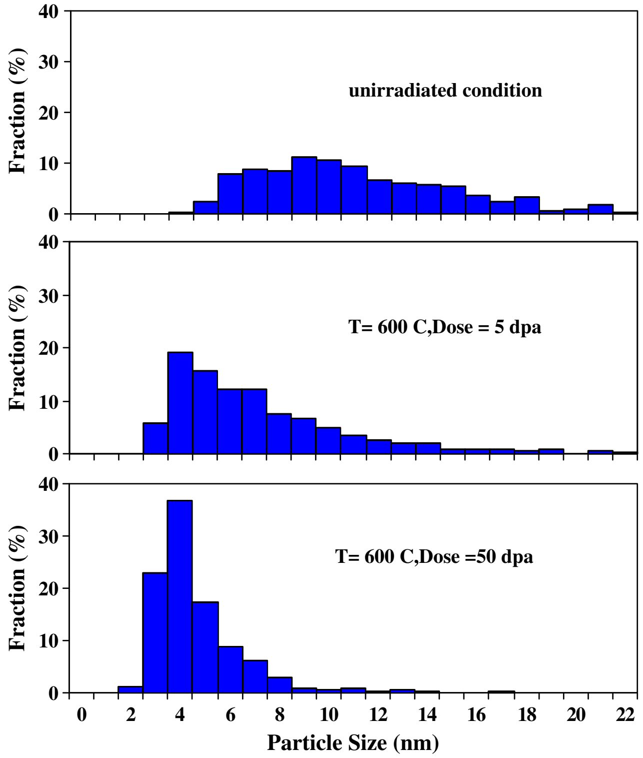

Fig. 9. Particle size (diameter) distribution for samples irradiated at 600 °C to doses of 0, 5, and 50 dpa.

doses, the measurable nanocluster volume decreases by approximately half. As will be explained, this is likely due to the remaining nanocluster particles becoming too small to measure using TEM. Fig. 7 shows an increase in measurable volume fraction for the 700 °C irradiation at 150 dpa. The cause of this increase has not been determined, but could be due to measurement uncertainties or to a recovery in particle size as the distributions move towards steady-state.

The particle size distribution as a function of dose is plotted in Figs. 8–10 for the 500, 600, and 700 °C irradiations, respectively. Due to TEM resolution limit on the images, particles smaller than 2 nm are not detected. To better quantify the smallest nanoclusters, electron energy loss spectroscopy (EELS) based techniques (an example is given in Kimura et al. [40]) should be used in future work. The unirradiated material has an average nanocluster size of 11.8 nm and is skewed right with tail toward larger size particles. At all three temperatures, as the radiation dose increases, the average size decreases and the larger size particles are removed from the matrix.

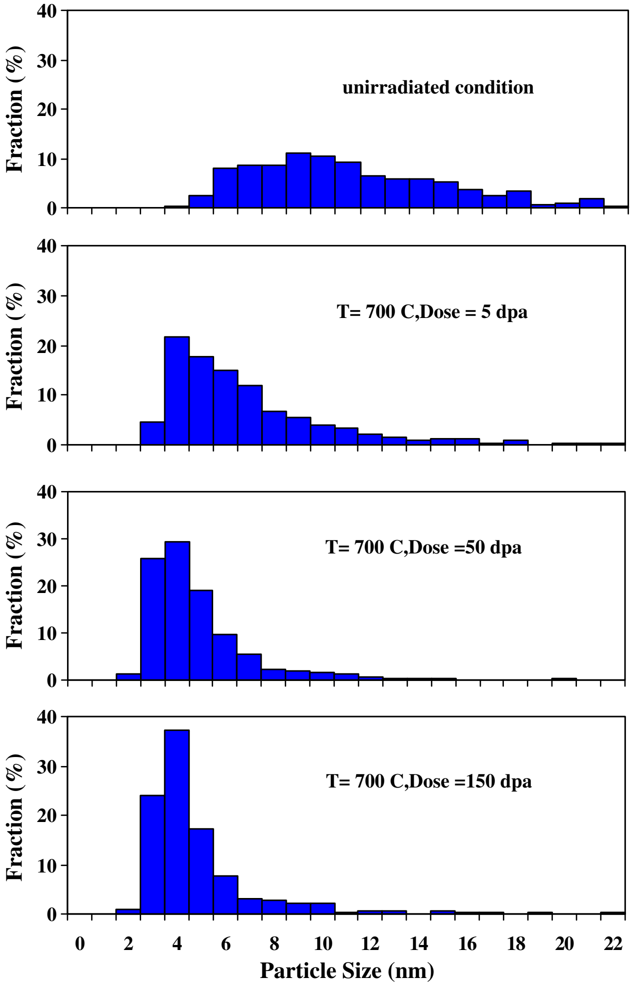

Fig. 10. Particle size (diameter) distribution for samples irradiated at 700 °C to doses of 0, 5, 50, and 150 dpa.

4. Discussion

4.1. Statistical analysis

Important details can be obtained by statistically analyzing the size distributions of the nanoclusters as a function of experimental temperature and dose. Skewness is a statistical measurement that characterizes the degree of asymmetry of a distribution around its mean. If the skewness value is positive, then the distribution has an asymmetric tail extending towards more positive values. If the skewness value is negative, the distribution has an asymmetric tail extending towards more negative values. Kurtosis describes the 'flatness' of a distribution when compared to a normal distribution. If a kurtosis value is positive, it indicates that the distribution is more peaked than a normal distribution. If the kurtosis value is negative, then it indicates that the distribution is flat compared to the normal distribution.

A statistical analysis of the nanocluster size distribution for the 500 °C irradiation is presented in Fig. 11. As the dose increases, the range of particle sizes becomes narrower. The smallest size particle observed does not change (this is a limitation of the measurement technique and not necessarily representing the actual smallest size nanocluster) but the larger particles are lost at higher dose. There are no apparent trends in skewness or kurtosis as a function of radiation dose.

A statistical analysis of the size distribution for the 600 and 700 °C irradiations is presented in Figs. 12 and 13. As the dose increases, the range of particle sizes becomes narrower. The larger particles are lost at higher dose. The skewness and kurtosis increase as a function of radiation dose, indicating a more prominent tail toward large particle sizes.

Earlier analysis of the nanocluster stability for samples irradiated at 500 °C indicated the particle size was reasonably described by a log-normal distribution [20]. Fig. 14 attempts the same analysis for the size distribution for unirradiated samples and for samples irradiated at 600 °C and 50 dpa. For the samples irradiated to 50 dpa, the log-normal distribution is not a good fit, especially at larger particle size. Fig. 15 compares the 700 °C 150 dpa nanocluster distribution to both a log-normal and half-normal distribution. Similar to the results at 600 °C, the log-normal is not a good fit at 700 °C. Although not an accurate fit, the half-normal distribution is a better fit for high temp, high dose samples. Assuming the lack of change in the lower limit of the size distribution for all irradiation conditions occurs because the particles become smaller than the TEM resolution, and noting that the distributions are 'reasonably' fit by half a normal distribution, a best estimate of the actual particle size distribution for the

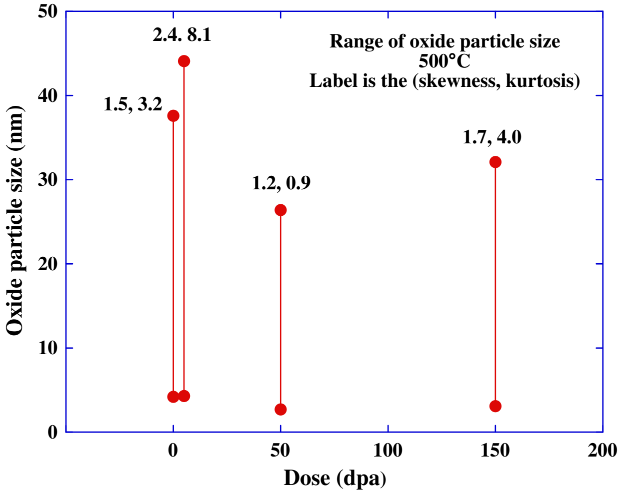

Fig. 11. Range of particle size (diameter), skewness, and kurtosis for samples irradiated at 500 °C to doses of 0, 5, 50, and 150 dpa.

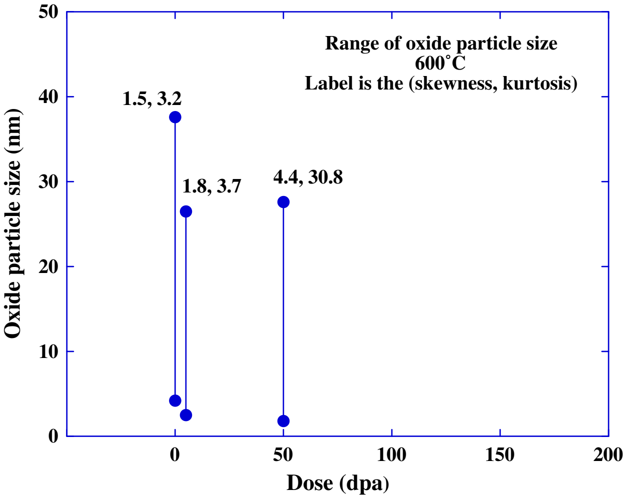

Fig. 12. Range of particle size (diameter), skewness, and kurtosis for samples irradiated at 600 °C to doses of 0, 5, and 50 dpa.

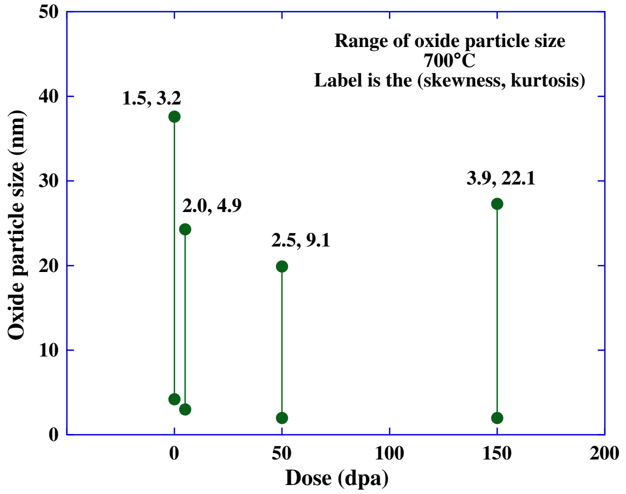

Fig. 13. Range of particle size (diameter), skewness, and kurtosis for samples irradiated at 700 °C to doses of 0, 5, 50, and 150 dpa.

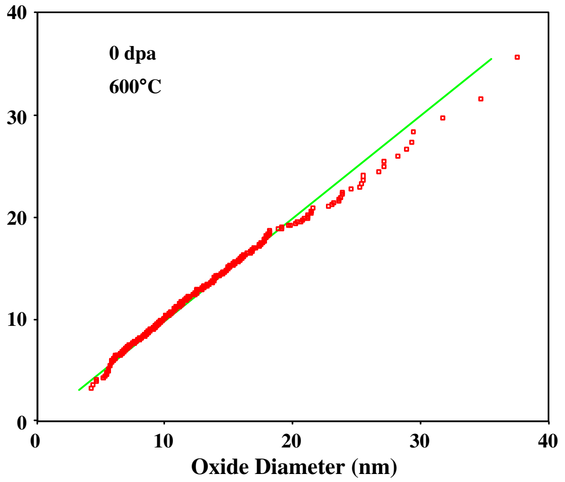

Fig. 14. Measured oxide particle diameter distribution for samples irradiated at 600 °C as compared to a log-normal distribution. The size distribution does not follow a log-normal distribution at high dose.

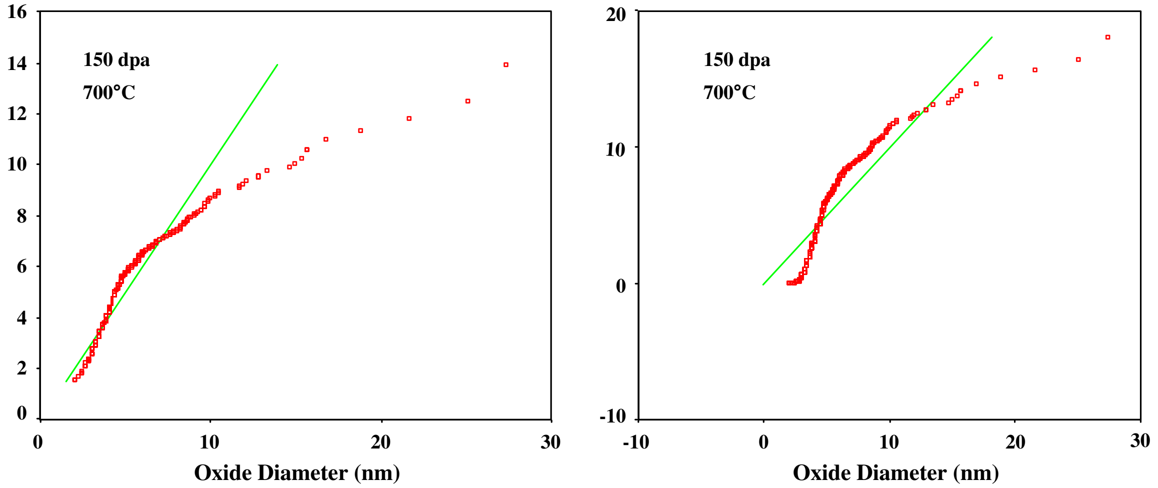

Fig. 15. Measured oxide particle diameter distribution for samples irradiated at 700 °C to 150 dpa as compared to a log-normal distribution (left) and a half-normal distribution (right). The size distribution does not follow either distribution well, but is better approximated by the half-normal distribution.

higher temperature irradiation conditions might actually be a normal distribution.

4.2. Effect of nanocluster size on strength

Dispersed hardening theory stipulates that the strength of a material is proportional to the inverse of the distance between dispersed obstacles ($\sqrt{Nd}$ where N is the obstacle density and d the average diameter) [3,21]. The percent change in Nd as a function of irradiation dose at all three irradiation temperatures is presented in Fig. 16. As a general trend, Nd increases indicate that even though radiation tends to decrease the average obstacle size, a shift toward a higher density of smaller obstacles under radiation should increase the ODS alloys strength at high radiation dose. If this result holds true across all radiation studies, ODS alloys hold great promise for holding strength to high radiation dose, a very valuable property.

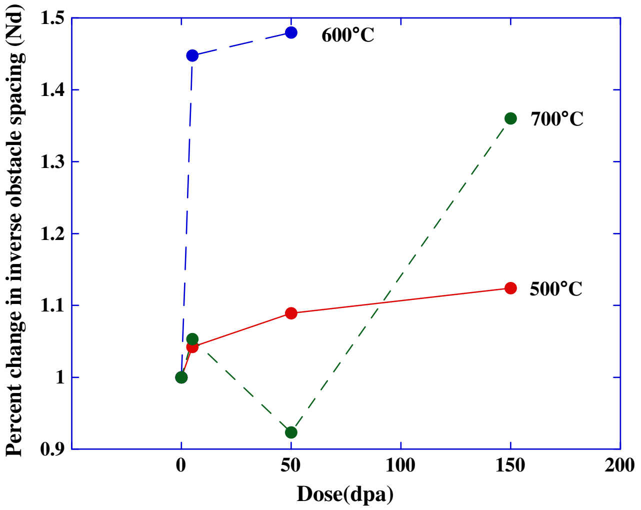

Fig. 16. Change in inverse square spacing between obstacles (Nd) for samples irradiated at 500, 600, and 700 °C.

4.3. Nanocluster stability as a function of irradiation conditions

The change in average nanocluster size as a function of radiation dose is very different between 500, 600, and 700 °C. This indicates that the reduction in size is not strictly a ballistic effect. Previous work showed that at 500 °C, the size reduction followed a square root of dose dependence consistent with ballistic mixing [20]. At higher temperatures, the square root of dose dependence no longer holds and the size reduction is accelerated.

A number of studies have irradiated different versions of ODS ferritic–martensitic steels using various ion beams, electrons, and neutrons, see Tables 3 and 4. A large number report that the oxide particles are stable under radiation (the term oxide is used here instead of nanocluster to be consistent with the references, but in many cases the material being irradiated likely had similar Y–Ti–O nanoclusters as the material irradiated in this study). A summary of these studies is listed in Table 3. Many of these studies were not primarily focused on oxide stability, but rather on void swelling response. Because of this focus, no data is reported on oxide size, but each paper mentions that the oxides were stable, at a minimum meaning they were still visible in some form following radiation. With the exception of the study by Asano et al., the studies reporting stable oxides were irradiated at lower temperature (450 °C or less), lower dose, or using low energy particles.

Table 3
Historical survey of yttrium–titanium-oxides reported to be stable under radiation

Author	Material	Irradiation particle	Temperature (°C)	Dose (dpa)	Dose rate (dpa/s)	Result
Pareige [22]	12YWT	150 keV Fe	300	0.7	1.9×10^{-4}	Stable dispersions
Asano [23]	MA957	1 MeV He (+) 4 MeV Ni	450 650	150	2×10^{-3}	Stable oxides
Hide [24]	MA957	42 keV He at 25 °C (+) 200 keV C$^-$	475 525 575 625	200	1.0–1.4 $\times 10^{-2}$	Stable oxides
Hide [24]	MA957	220 keV He at 25 °C (+) 3 MeV Ni$^+$	475 525	150	3.0×10^{-3}	Stable oxides
Little [25]	DT2203YO5	52 MeV Cr^{6+} (+) 4 MeV He	475	50	3.0×10^{-4}	Stable oxides
Saito [26]	13Cr–0.5TiO$_2$–0.2Y$_2$O$_3$	1 MeV electron	400 500	12	2.2×10^{-3}	Stable oxides
Kinoshita [27]	13Cr ODS (+) Nb, V, Zr	1 MeV electron	350 450	15	2×10^{-3}	Stable oxides
Akasaka [28]	9Cr and 12 Cr ODS	Fast neutrons (JOYO)	330 400 450 500	7.0 2.5 14.0 15.0	Not reported[a]	Stable oxides
Mathon [29]	MA957	Thermal neutrons (OSIRIS)	325	0.8, 2.0, 3.5, 5.5	1×10^{14} n/cm^2 ($E > 1$ MeV) σ_f–σ_{th}	Stable dispersions
Monnet [32]	DY EM10 + Y2O3 EM10 + MgO	1 MeV Helium	400	0.05	Not reported	No change in oxide particles
Kimura [39]	(13–19)Cr–4Al ODS		300–500	20	~1×10^{-4}	No reported change in oxide size

[a] Typical fast reactor displacement rates in the driver fuel portion of the core are ~1×10^{-6} dpa/s.

Table 4
Historical survey of yttrium–titanium-oxides reported change size under radiation

Author	Material	Irradiation particle	Temperature (°C)	Dose (dpa)	Dose rate (dpa/s)	Result
Yamashita [30]	IDS (11Cr) and IDK (13 Cr)	Fast Neutron (JOYO)	450–561	21	Not reported[a]	Small particles disappear. Average particles increase slightly with increasing temp or dose
Dubuisson [31]	DT2203YO5	Fast neutron (PHENIX)	400–580	81	Not reported[a]	Oxide particles are totally dissolved (small oxides) or reduced in size and were surrounded by a halo of smaller oxides (large oxides)
Monnet [32]	DT2203YO5	Fast neutron (PHENIX)	400–580	81	Not reported[a]	Disappearance of small oxides and significant halo of smaller oxides at higher temperatures and doses
Monnet [32]	DY EM10 + Y2O3 EM10 + MgO	1 MeV and 1.2 MeV Electron	300–550	100	3–6 $\times 10^{-3}$	Oxides stable at 400 °C under 1.0 MeV electrons but dissolve under 1.2 MeV

[a] Typical fast reactor displacement rates in the driver fuel portion of the core are ~1×10^{-6} dpa/s.

In this work, nanoclusters were shown to decrease in size as a function of radiation, with the decrease occurring faster at 600 and 700 °C, as compared to the decrease in size that occurs at 500 °C. Dissolution of the nanoclusters at higher temperatures and doses has also been found in other studies. Dubuisson [31] and Monnet [32] studied the oxide stability of DT2203YO5 irradiated in the PHENIX fast reactor over a range of temperatures from 400–580 °C and to doses as high as 81 dpa. Small oxides dissolved under radiation at higher temperatures and doses, but did not dissolve at lower irradiation dose. Their data is reproduced in Fig. 17. For larger oxides, a halo of small oxides was formed around the larger oxide particles for all conditions where the smaller oxides dissolved. This halo was on the order of 80–100 nm in width. Faint, smaller halos were found in the irradiation conditions where small particles appeared stable. No similar halos were identified in the samples ion irradiated in this work. Yamashita [30] studied oxide stability in material irradiated in the JOYO fast reactor at temperatures from 450–561 °C to doses of 21 dpa. Yamashita found that small particles disappear and average particles increase slightly in size with increasing temp or dose.

Monnet supplemented the neutron radiation studies with electron irradiations of yttrium oxides and magnesium oxides in the EM10 alloy at temperatures between 300 and 550 °C and to doses of 100 dpa. In these studies, the yttrium oxides were stable at 400 °C when irradiated with 1.0 MeV electrons but dissolved under 1.2 MeV electron irradiation. Yttrium oxides showed less dissolution than the magnesium oxides. The authors proposed that a minimum displacement energy, sufficient to displace both metal and oxide atoms from the lattice, is required to make dissolution possible. For the oxide dissolution that occurred with the 1.2 MeV electrons, the radius loss was linear with increasing dose.

To determine the high temperature stability of yttrium–titanium oxides, Miller et al. [15] studied the stability of the oxides at 1300 °C for 24 h and found that at high temperature and no radiation, limited coarsening occurred.

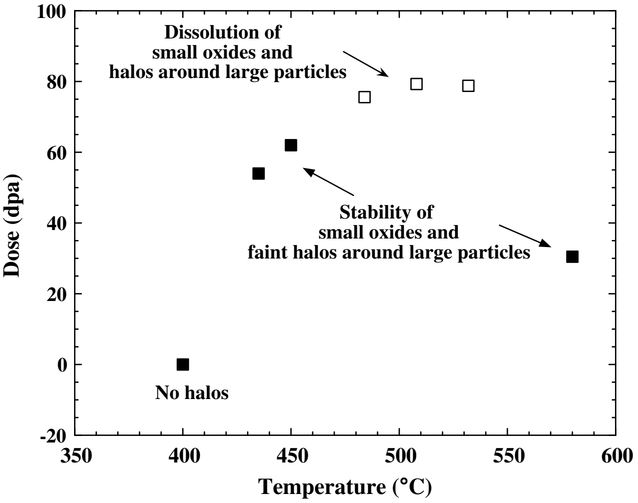

Fig. 17. Oxide dissolution data from Ref. [32].

In summary, the following trends appear to occur relative to nanocluster stability:

- Nanoclusters are relatively stable at temperatures approaching the melting point, undergoing limited coarsening only [15].
- Nanocluster size decreases at higher temperatures and higher radiation doses. For Ni-ion irradiation, the decrease in size is faster at 600 and 700 °C than at 500 °C. This indicates a diffusion-based mechanism is involved in the dissolution.
- Oxide dissolution was linear with dose for low temperature electron irradiations (Ref. [32]) but faster than linear when exposed to higher temperature Ni-ion irradiation (this work).
- A minimum displacement energy may be required that is high enough to displace both metal and oxide atoms in the oxide particle [32].
- Halos of smaller oxide particles around large oxides have only been reported in the PHENIX radiations [31].

A few issues must be considered when comparing stability of clusters using different irradiation techniques:

- Each radiation technique leads to a different collision cascade size. Electron radiation can only displace single atoms where heavy ions and neutrons can lead to cascades that disrupt a large fraction of atoms in the nanocluster. Mechanistically, different effects are expected when using electron irradiation so a direct comparison to heavy ion irradiation may help elucidate mechanisms of dissolution.
- Heavy ion beam techniques inject additional ions into the matrix that have the potential to change local chemistries and the associated local diffusion rates. Ideally, samples will be prepared from regions of the sample away from the large number of injected interstitial atoms. The studies reported here that use heavy ions do not generally report the location of sample preparation within the irradiated zone making conclusions based on injected atoms not possible.
- Radiation-enhanced diffusion depends on available migrating point defects [33], the concentration of which is temperature and displacement rate dependent. Mansur [34] describes techniques for estimating the shifts in temperature or displacement rate required to gain equivalence in radiation techniques. Put in the simplest terms, irradiation at higher rate requires a higher temperature to obtain comparable radiation environments. Examining the results of this work alongside the summary of data in Tables 3 and 4, oxide clusters shrink only under during high temperature neutron radiation and higher temperature heavy ion irradiation. The dissolution may be possible via a mechanism that occurs only in certain temperature and dose rate regimes where diffusion is significant.

- The use of rastered versus non-rastered beams affects the effective displacement rate. For rastered systems, the portion of the target being irradiated is only bombarded for a fraction of the time, thus leading to a high local displacement rate followed by a significant period of annealing. The net effect is a lower displacement rate for the same beam current being applied in a non-rastered mode [35]. The studies reported do not generally report whether the beam was rastered or not, making conclusions based on raster profile not possible.

4.4. Mechanism of dissolution

Russell presented the theory of precipitate stability under radiation [36]. In general, a particle that is ballistically ejected from an oxide can:

- Back-diffuse to rejoin the original particle
- Diffuse to join another particle
- Help nucleate a new particle
- Remain in solution in the matrix

Russell presented an equation for the time rate of change of the radius of a particle under radiation assuming a volume loss due to recoil dissolution or disordering dissolution as well as particle growth due to diffusion from solution

$$\frac{\mathrm{d}r}{\mathrm{d}\phi} \cong -\frac{\xi}{N} + \frac{3D}{4\pi r K}\frac{C_\mathrm{t}}{C_\mathrm{p}} - \frac{Dr^2 n}{K}, \tag{1}$$

where r is the particle radius; σ, the dose (dpa); K, the dose rate (dpa/s); ξ/N, the radius loss due to ballistic collisions due to radiation; D, the diffusion coefficient; C_t, the total solute concentration; C_p, the concentration of the solute in precipitates; (C_t–C_p, the remaining concentration in solution) and n is the density of precipitates (number per unit volume) in the matrix.

Thus, precipitates can grow through diffusion of solute from the matrix (second term in Eq. (1)) or can shrink due to radiation-induced recoils (first term in Eq. (1)) or through release and diffusion of solute to other precipitates (third term in Eq. (1)). For a precipitate described by Eq. (1), large particles would shrink and small particles would grow, leading to a stable radius that depends on the dissolution constant (ξ), the displacement rate (K), and the diffusion coefficient (D). The diffusion coefficient would be the radiation-enhanced diffusion coefficient. The theory predicts that particles would dissolve under radiation at lower temperatures because sufficient diffusion cannot occur to re-precipitate. A critical temperature would exist above which dissolution is negligible as diffusion would be rapid enough to maintain large precipitates. Russell noted that in systems with limited solubility (C_t and C_p approximately equal), dissolution would break up the particles into a set of finer particles.

For the yttrium–titanium nanoclusters studied in this work and reported in the literature, the literature does not consistently indicate size reduction of the nanoclusters. Size reduction generally shows up only at higher temperature and dose. The following bullet points are provided to try and describe the trends seen in those studies where reduction does occur:

- Dissolution can create particles too small to be imaged using bright field TEM. This is noted in the loss of imagable volume plotted in Fig. 7. Nonetheless, the size distributions appear to be reaching a stable size at 600 and 700 °C while still decreasing in size at a slower rate at 500 °C.
- The size of the cascades is similar to the size of the oxide particles. Where the theory in Eq. (1) assumes large particles for which any specific cascade can only ballistically remove a portion of the oxide, for nanometer-sized nanoclusters, the cascades from a Ni-ion irradiation can disrupt the structure of the entire nanocluster. Since halos around oxide particles have only been seen on larger (~200 nm) oxides, the smaller oxides are likely to be near fully disrupted by collision cascades.
- Prior to irradiation, the density of particles (n) is small such that the third term in Eq. (1) is very small compared to the first and second. Loss of volume from one precipitate to another is not likely early in the radiation. This can change in regions local to an existing precipitate if smaller surrounding precipitates are formed due to the radiation.
- Between 0 and 5 dpa, the rate of radius loss increases with temperature so the mechanism leading to loss of particle radius is more complicated than simple radiation-induced ballistic dissolution. Simple radiation-induced ballistic dissolution would lead to a linear loss rate with respect to dose.
- Dissolution occurs faster at higher temperature, the opposite of that predicted by Eq. (1). Therefore, diffusion is likely to be critical. Careful comparison of oxide nanocluster dissolution under ion and electron radiation (where electrons cannot cause cascades) would help to elucidate this question.
- The displacement energy for Y and O in an yttrium-oxide are 57 eV [37,38] while that for iron is 40 eV. Assuming similar displacement energies in the Y–Ti–O nanoclusters, the radiation-induced vacancy concentration should be larger in the metal matrix providing a driving force for a net vacancy flux to the precipitate. This could drive the precipitate mass loss if vacancy absorption frees a precipitate atom (rather than growing the precipitate by adding an atom to the surface and creating a more porous participate). Based on the electron irradiation work [32], both the metal and oxygen atom must be displaced for oxides to shrink.
- If radiation-induced diffusion of point defects is critical to the oxide dissolution, then a radiation-induced segregation profile is expected at the surface of the nanoparticle. Work is underway to try and measure this segregation.

5. Conclusions

Ferritic–martensitic (FM) alloys are expected to play an important role as cladding or structural components in Generation IV systems. Oxide dispersion strengthened ferritic–martensitic steels have been developed to operate at higher temperatures than traditional FM steels. Heavy ion irradiation has been used to determine the oxide stability in a 9Cr martensitic steel strengthened with nanometer scale dispersions of Y–Ti–O particles. The ODS steel was irradiated over a temperature range of 500–700 °C to doses of 150 dpa. At all temperatures, the average oxide size decreases but the oxide density increases. The increased density of smaller oxide particles under radiation should lead to strengthening of the matrix. The changes in oxide size are not entirely driven by ballistic processes but are strongly temperature dependent.

Acknowledgements

Research at the Oak Ridge National Laboratory SHaRE User Facility was sponsored by Basic Energy Sciences, US Department of Energy. The ODS sample material was generously provided by the Japan Atomic Energy Agency.

References

[1] A Technology Roadmap for Generation IV Nuclear Energy Systems, US DOE Nuclear Energy Research Advisory Committee and the Generation IV International Forum, December (2002).
[2] D.S. Gelles, DOE/ER-0313/16, March 1994, p. 146.
[3] S. Yamashita, K. Oka, S. Ohnuki, N. Akasaka, S. Ukai, J. Nucl. Mater. 307–311 (2002) 283.
[4] S. Ohtuska, S. Ukai, M. Fujiwara, T. Kaito, T. Narita, Mater. Trans. 46 (3) (2005) 1.
[5] T.F. Kelly, M.K. Miller, Rev. Sci. Instrum. 78 (2007) 031101.
[6] J.M. Hyde, C.A. English, in: G.E. Lucas, L. Snead, M.A. Kirk Jr., R.G. Elliman (Eds.), Proceedings MRS 000 Fall Meeting, Symposium R: Microstructural processes in irradiated materials, Boston, MA, November 27–30, 2000, vol. 650, Materials Research Society, Pittsburgh, PA, 2001, p. R6.6.1.
[7] J.P. Huchra, M.J. Geller, ApJ 257 (1982) 423.
[8] M.K. Miller, Atom Probe Tomography, Kluwer Academic/Plenum, New York, NY, 2000.
[9] J.F. Ziegler, J.P. Biersack, SRIM-2003 Program, IBM Corp.,Yorktown, NY.
[10] M.K. Miller, E.A. Kenik, K.F. Russell, L. Heatherly, D.T. Hoelzer, P.J. Maziasz, Mater. Sci. Eng. A A353 (2003) 140.
[11] E.A. Kenik, D. Hoelzer, P.J. Maziasz, M.K. Miller, Microsc. Microanal. 7 (2001) 550.
[12] M.K. Miller, D. Hoelzer, E.A. Kenik, K.F. Russell, Micros. Microanal. 9 (Suppl. 2) (2003) 44.
[13] M.K. Miller, D.T. Hoelzer, E.A. Kenik, K.F. Russell, J. Nucl. Mater. 329–333 (2004) 338.
[14] M.K. Miller, D.T. Hoelzer, E.A. Kenik, K.F. Russell, Microsc. Microanal. 10 (Suppl. 2) (2004) 708CD.
[15] M.K. Miller, D.T. Hoelzer, E.A. Kenik, K.F. Russell, Intermetallics 13 (2005) 387.
[16] M.K. Miller, K.F. Russell, D.T. Hoelzer, J. Nucl. Mater. 351 (2006) 261.
[17] T.R. Allen, L. Tan, J.D. Tucker, J. Gan, G. Gupta, G.S. Was, S. Shutthanandan, S. Thevuthasan, J. ASTM Int. 2 (8) (September 2005), Paper ID JAI12382.
[18] T.R. Allen, L. Tan, Y. Chen, K. Sridharan, M.T. Machut, J. Gan, G. Gupta, G.S. Was, S. Ukai, in: Proceedings of Global 2005, Paper IL001.
[19] S. Yamashita, N. Akasaka, S. Ohnuki, J. Nucl. Mater. 329–333 (2004) 377.
[20] T.R. Allen, J. Gan, J.I. Cole, S. Ukai, S. Shutthanandan, S. Thevuthasan, Nucl. Sci. Eng. 151 (2005) 305.
[21] D.A. Porter, K.E. Easterling, Phase Transformations in Metals and Alloys, Chapman and Hall, 1992.
[22] P. Pareige, M.K. Miller, R.E. Stoller, D.T. Hoelzer, E. Cadel, B. Radiguet, J. Nucl. Mater. 360 (2007) 136.
[23] K. Asano, Y. Kohno, A. Kohyama, T. Suzuki, H. Kusanagi, J. Nucl. Mater. 155–157 (1988) 928.
[24] K. Hide, N. Sekimura, K. Fukuya, H. Kusanagi, M. Taguchi, T. Satake, Y. Arai, M. Iimuna, H. Takaku, S. Ishino, in: N.H. Packan, R.E. Stoller, A.S. Kumar, (Eds.), Effects of Radiation on Materials: 14th International Symposium, vol. I. ASTM STP 1046. American Society for Testing and Materials, p. 61.
[25] E.A. Little, in: D.S. Gelles, R.K. Nanstad, A.S. Kumar, E.A. Little, (Eds.), Effects of Radiation on Materials: 17th International Symposium, ASTM STP 1270, American Society for Testing and Materials, p. 739.
[26] J. Saito, T. Suda, S. Yamashita, S. Ohnuki, H. Takahashi, N. Akasaka, M. Nishida, S. Ukai, J. Nucl. Mater. 258–263 (1998) 1264.
[27] H. Kinoshita, N. Akasaka, H. Takahashi, I. Shibahara, S. Onose, J. Nucl. Mater. 191–194 (1992) 874.
[28] N. Akasaka, S. Yamashita, T. Yoshitake, S. Ukai, A. Kimura, J. Nucl. Mater. 329–333 (2004) 1053.
[29] M.-H. Mathon, Y. de Carlan, X. Averty, Ch-H. Alamo, de Novion, J. ASTM Int. 2 (8) (2005), Paper ID JAI 12381.
[30] S. Yamashita, K. Oka, S. Ohnuki, N. Akasaka, S. Ukai, J. Nucl. Mater. 307–311 (2002) 283.
[31] P. Dubuisson, R. Schill, M.-P. Higon, I. Grislin, J.-L. Seran, in: R.K. Nanstad, M.L. Hamilton, F.A. Garner, A.S. Kumar (Eds.), Effects of Radiation on Materials: 18th International Symposium, ASTM STP 1325, American Society for Testing and Materials, p. 882.
[32] I. Monnet, P. Dubuisson, Y. Serruys, M.O. Ruault, O. Kaitasov, B. Jouffrey, J. Nucl. Mater. 335 (2004) 311.
[33] S.J. Zinkle, B.N. Singh, J. Nucl. Mater. 199 (1993) 173.
[34] L.K. Mansur, Nucl. Tech. 40 (1978) 5.
[35] G.S. Was, Fundamentals of Radiation Materials Science: Metals and Alloys, Springer, 2007, p. 557.
[36] K.C. Russell, J. Nucl. Mater. 206 (1993) 129.
[37] M.D. Rechtin, H. Wiedersich, Radiat. Eff. 31 (1977) 181.
[38] S.J. Zinkle, C. Kinoshita, J. Nucl. Mater. 251 (1997) 200.
[39] A. Kimura, H. Cho, N. Toda, R. Kasada, K. Yutani, H. Kishimoto, N. Iwata, S. Ukai, M. Fujiwara, J. Nucl. Sci. Technol. 44 (3) (2007) 323.
[40] C. Bonafos, B. Garrido, M. Lopez, A. Perez-Rodriguez, J.R. Morante, Y. Kihn, G. Ben Assayag, A. Claverie, Appl. Phys. Lett. 76 (26) (2000) 3962.